## Adaptive mesh refinement for simulating unsteady bow wave breaking

Jahra, Fatima; Seo, Dong Cheol

# ADAPTIVE MESH REFINEMENT FOR SIMULATING UNSTEADY BOW WAVE BREAKING

**Fatima Jahra (National Research Council Canada, Canada)**
**Dong Cheol Seo (National Research Council Canada, Canada)**

## 1. ABSTRACT

Wave breaking around marine vessels, particularly in the bow region, plays a critical role in determining hydrodynamic resistance and overall performance. This study investigates the complex bow wave breaking phenomenon using the KRISO Container Ship (KCS) model as a reference hull. Computational Fluid Dynamics (CFD) analyses were performed with two commercial solvers, STAR-CCM+ and ANSYS FLUENT, with a focus on accurately capturing unsteady bow wave breaking. The paper highlights the detailed numerical setups developed to enhance simulation performance in resolving unsteady wave breaking behaviour. The CFD results are compared with experimental model test data to evaluate simulation accuracy and confirm their reliability.

## 2. INTRODUCTION

Vessel performance at sea is influenced by the wave breaking characteristics of that vessel. Wave breaking phenomena around the hull influences the hydrodynamic performance of the vessel in terms of resistance, manoeuvring, and seakeeping performance. Therefore, analysing or evaluation of the wave breaking characteristics is indispensable for hull performance analysis and for optimization of the hull design at the design stage of the vessel.

Wave breaking commonly occurs in the bow and stern areas of a ship at sea and involves complex two-phase flow and unsteady hydrodynamic phenomena, which is challenging for both CFD simulations and physical understanding [1].

Several studies have investigated the wave breaking characteristics of various hull forms through physical model tests and numerical analysis. In the late 1960's, Baba [2] examined the influence of wave breaking on hull resistance. Hengelmolen and Wellens [3] studied the effect of bow wave breaking on added resistance through physical experiments that combined visual observations with resistance tests. They also introduced a novel waterline detection method based on stereo vision, which relies on the semi-transparency of the ship hull to measure how the relative wave elevation in the bow region exhibits nonlinear behaviour. Choi et. al. [4] experimentally investigated the effect of bow wave breaking of a fast displacement ship in waves and provided an insight into the nonlinear relationship between relative wave elevation and added resistance. They also discussed the process of plunging in the breaking of bow waves.

With advances in modelling techniques and computing power, CFD has become increasingly popular due to its cost- and time-effectiveness compared to physical model tests and sea trials. However, CFD predictions must be validated against physical tests or full-scale trial data to ensure their reliability. Once validated, CFD can be applied to simulate a wide range of scenarios that would otherwise be prohibitively expensive to investigate experimentally.

Several researchers have applied CFD to predict the bow, shoulder and stern wave-breaking phenomena, followed by extensive CFD model validation process. Di Mascio et al. [5] presented one of the first RANS based simulations of breaking waves for a practical ship geometry using a surface capturing single-phase level set method. Olivieri et. al. [6] conducted a detailed study on bow and shoulder wave-breaking phenomena of the DTMB Model 5415 surface combatant, combining physical model test data with CFD validation. Their study found that the number of induced vortices and free surface scars depended on both hull form and Froude number (Fr), with scars associated with sudden changes in the mean wave height and vortices generated by wave breaking. They also presented the near- and far-field measurements of mean and RMS wave elevations as well as mean velocities under the breaking waves, showing a direct correlation between the regions with wave slopes greater than 17 degrees and the areas with large RMS variations in wave elevation. Wilson et. al. [7] applied an unsteady Reynolds-Averaged Navier–Stokes (URANS) solver (CFDSHIP-IOWA) to study wave breaking characteristics of the high-speed transom stern ship, R/V Athena I, at three different speeds. They reported that at high Froude number (i.e., $Fr=0.62$), intense bow wave breaking occurred, with repeated reconnection of the plunging breakers with the free surface, generating multiple free surface scars. Lin and Percival [8] also performed RANS simulation for the R/V Athena geometry over a range of speeds ($0.28 < Fr < 0.48$), but their free surface model did not capture wave breaking, resulting in poor agreement with experiments at higher Froude numbers. Demonstrating that the wave breaking characteristics depend on hull form, Wang et al. [9] observed more violent plunging type bow wave breaking for the KCS hull than for the DTMB 5415 surface combatant in their combined experimental and numerical study. Xu et. al. [10]

applied a smoothed particle hydrodynamics (SPH) method under the Lagrange framework to simulate the bow wave breaking on the KCS model at four different speeds (*Fr = 0.35, 0.40, 0.50 and 0.60*). Their results showed that the SPH method successfully captured different types of wave breaking (spilling breakers, plunging breakers, and free-surface scars) with reasonable agreement with experimental data. Finally, Simonsen et al. [11] investigated the added resistance of the KCS model in calm water and regular waves using CFDSHIP-IOWA and Star-CCM+, comparing the time series of experimental and simulated resistance data.

This study aims to improve the simulation of bow wave breaking using two commercial CFD packages, STAR-CCM+ and Fluent, with the KCS hull as the test case. The simulation results are compared with physical model tests conducted by the China Ship Scientific Research Center (CSSRC). This paper is intended for submission to Wageningen 2025: A Workshop on CFD in Ship Hydrodynamics. However, given the workshop's emphasis on inter-participant comparisons, the paper focuses primarily on the details of the applied simulation setups rather than on a comprehensive comparison of results.

## 3. GENERAL DESCRIPTION OF CONDUCTED CFD SIMULATION

In this study, a model-scale KCS hull form (1:37.89) was used [1]. The CAD geometry was provided by the organizers of the W2025 Workshop on CFD Ship Hydrodynamics. The model was trimmed 1° by the bow, with both trim and sinkage fixed during the test. The simulation conditions were matched to those of the physical model tests conducted by CSSRC [1], including the test speed (*Fr=0.35*).

### 3.1 Numerical approach

In this study, two commercial CFD codes, SIEMENS Star-CCM+ and ANSYS FLUENT, were employed. The aim was to evaluate their simulation performance under nearly identical conditions. However, a systematic comparison was not feasible due to internal constraints, such as differences in hardware capabilities and license configurations, which limited the grid resolution and the choice of numerical schemes. While the simulation outcomes do not support a systematic comparison, a qualitative comparison and discussion of simulation performance between the two CFD packages is provided. Details of the applied simulation setup for each code will be presented separately.

Table 1 Tested CFD solvers and versions.

| Solver | Star-CCM+ | FLUENT |
|---|---|---|
| Software version | 2406 | 2024 R1 |
| Number of cores used | 60 | 12 |

### 3.2 Numerical Schemes

Applied numerical schemes and methods are summarized in Table 2. In this study, an URANS solver was employed in conjunction with SST k-ω model. The free-surface interface was tracked using the Volume of Fluid (VOF) method in both CFD packages. However, Star-CCM+ utilized the Modified High-Resolution Interface Capturing (MHRIC) scheme, whereas FLUENT employed a compressive interface-capturing scheme. For pressure–velocity coupling, the Semi-Implicit Method for Pressure-Linked Equations (SIMPLE) was adopted in Star-CCM+, while the coupled method was applied in FLUENT. Other numerical models, such as the All y+ Wall Treatment, were implemented in a nearly identical manner in both solvers. The time step size was slightly adjusted based on the grid resolution, as discussed in the following section.

For all simulations, the water properties were set based on the case description, with a water temperature of 15°C, density of 999.1026 kg/m$^3$, and kinematic viscosity of $1.1386\times10^{-6}$ m$^2$/s [1].

### 3.3 Computational Domain

The CFD simulations were performed at model scale using a half-body model to reduce computational cost. The computational domain configuration and the applied boundary conditions are shown in Figure 1, while the detailed domain dimensions are provided in Table 4. Due to limitations in available CPU cores, a slightly smaller computational domain was employed for the FLUENT simulations compared to Star-CCM+.

### 3.4 Grid Generation

The main focus of this study is to evaluate the potential benefits of employing an Adaptive Mesh Refinement (AMR) model. Wave-breaking events, in particular, present an ideal case for AMR, as a very fine grid is required only in the vicinity of the free-surface interface. Furthermore, the exact location of the wave-breaking region is unknown prior to running the simulation and the specific location of free surface interface can change over time due to the inherent unsteadiness in wave breaking. This makes AMR especially advantageous, as it can dynamically adjust grid resolution to capture these transient and localized phenomena with greater accuracy and computational efficiency.

The summary of the constructed grids is presented in Table 4, while the minimum grid sizes are compared in Table 5. The calculated wall $y+$ values form both software are presented in Figure 2. Figure 3, Figure 4 and Figure 5 show the constructed grids for Star-CCM+ and FLUENT. For Star-CCM+, a trimmed mesher was employed, whereas a hybrid Polyhexcore mesher was used in FLUENT, combining structured hexahedral (hex) elements in the bulk region with polyhedral elements near the boundaries. In both CFD cases, prismatic layers were generated around the hull surfaces to better resolve near-wall flow behaviour. It should be noted that the reported values for Star-CCM+ were obtained after applying the AMR method; as a result, the grid statistics differ from those of the initial mesh configuration prior to AMR activation as shown in Figure 6.

Table 2 Summary of applied numerical schemes.

| | Star-CCM+ | FLUENT |
|---|---|---|
| Turbulence model | SST-K omega | SST-K omega |
| VOF interface capturing | Modified HRIC | Compressive |
| Interface capturing option | High interface sharpness | Sharp/dispersed |
| Pr-velocity coupling scheme | SIMPLE | Coupled |
| Spatial discretization | 2nd order upwind | 2nd order upwind |
| Temporal discretization | 1st order | 1st order |
| Time step size | 0.002 sec | 0.005 sec |
| Wave damping | Outlet (1 ship length) | Outlet (1 ship length) |

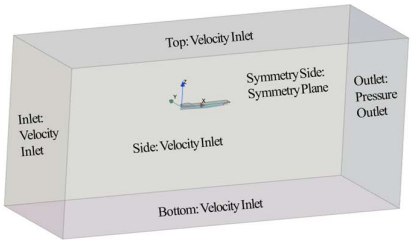


Figure 1 Computational Domain of KCS model.

Table 3 Computational Domain dimensions.

| | Star-CCM+ | FLUENT |
|---|---|---|
| X direction | -2.5 ~ 4.9 L | -1.0 ~ 3.0 L |
| Y direction | 0 ~ 1.0 L | 0 ~ 1.2 L |
| Z direction | -2.5 ~ 1.0 L | -1.0 ~ 0.5 L |

(L: ship length)

Table 4 Summary of constructed grids.

| | Star-CCM+ | FLUENT |
|---|---|---|
| Adaptive mesh | Yes | No |
| Grid type | Unstructured, Hexahedral (trimmed) mesh | Unstructured, Hybrid: Poly core and Hexahedral mesh |
| No. of volume element | 13.7 x $10^6$ (3.4 x $10^6$ without AMR) | 8.2 x $10^6$ |
| No. of surface element on main hull | 50,927 | 63,050 |
| Volumetric refinement around free surface | Antistrophic $\Delta x : \Delta y : \Delta z = 2:1:1$ | Isotropic |
| Hull averaged Y+ | 54.22 | 31.20 |

Table 5 Minimum grid size around wave breaking region.

| | Star-CCM+ | FLUENT |
|---|---|---|
| X [m] | 0.003 | 0.006 |
| Y [m] | 0.003 | 0.006 |
| Z [m] | 0.003 | 0.006 |

For the AMR setup in Star-CCM+, the maximum refinement level was set to three, with a user-defined minimum adaptation cell size specified to focus grid resolution on the targeted wave-breaking region while preventing excessive refinement in areas away from the ship, as summarized in Table 5.

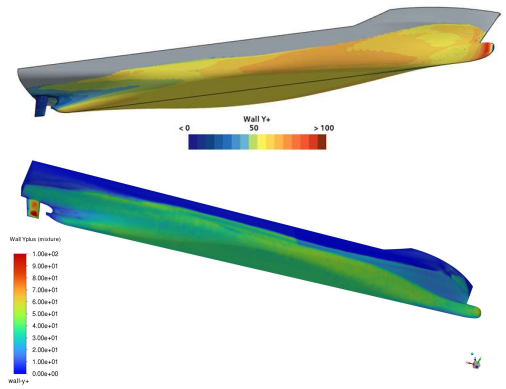


Figure 2 Wall $y+$ contours using Star-CCM+ (top) and FLUENT (bottom).

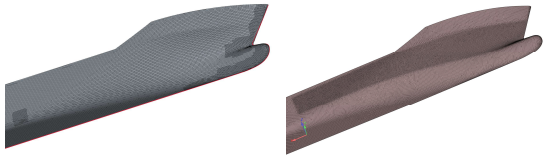

Figure 3 Initially constructed surface grids around bow area for Star-CCM+ (left) and FLUENT (right).

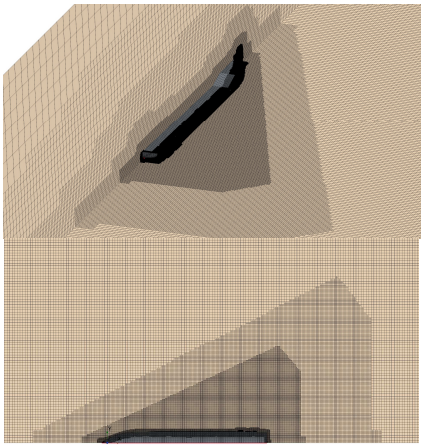

Figure 4 Iso and top view of initially generated grids for Star-CCM+.

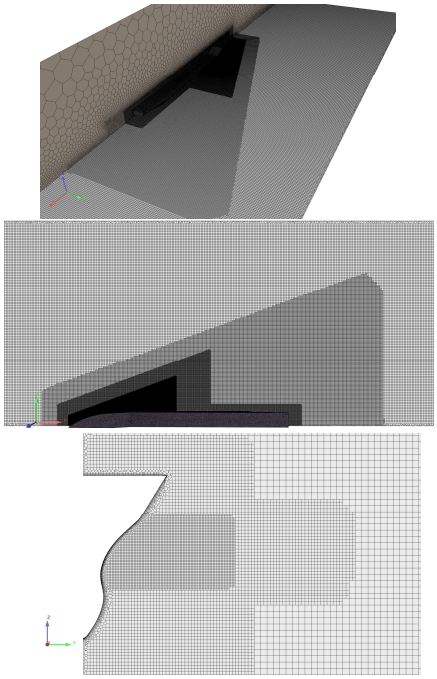

Figure 5 Iso, top and front view of generated grids for FLUENT.

Table 6 Implemented adaptive cell size control for Star-CCM+.

| X | | Y | | Min. Adaptive |
|---|---|---|---|---|
| Min | Max | Min | Max | Cell Size |
| -0.2 L | 1.2 L | 0 | 0.25 L | 0.004 m |
| -0.4 L | 1.6 L | 0 | 0.7 L | 0.01 m |

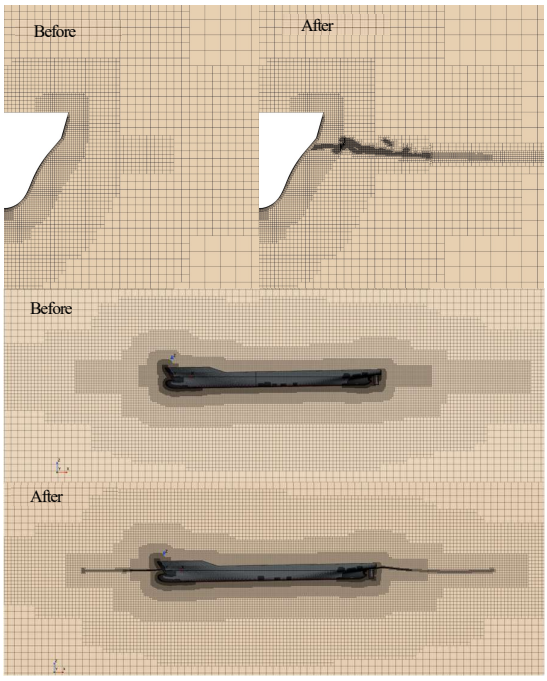


Figure 6 Typical example of grid refinements before and after applying AMR using Star-CCM+.

## 4. RESULTS AND DISCUSSIONS

The main simulation outcomes were prepared and submitted separately in accordance with the case description for further analysis. This paper presents only the most notable findings, which will be discussed in a later section.

### 4.1 Total Resistance, Heave Force, and Pitch Moment

The estimated hydrodynamic forces are summarized in Table 7 and compared with the model test data for the hull, as provided in the case description document. Both CFD packages predicted the total resistance and heave force coefficients in good agreement with the experimental measurements, with errors of less than 1% roughly. However, a significant discrepancy of approximately 20% was observed for the pitch moment. Both Star-CCM+ and FLUENT underpredicted the pitch moment. Given the relatively small order of magnitude of the pitch moment compared to the resistance or heave force, this large relative error is likely influenced by the numerical resolution challenges associated with accurately calculating values close to zero.

Figure 7 and Figure 8 present a direct comparison of the hydrodynamic forces and pitch moment coefficients predicted by the two CFD codes. The force and moment data were sampled over an 8-second period (approximately one cycle) after the flow reached a steady state. Star-CCM+ demonstrated more pronounced oscillatory behaviours, whereas FLUENT produced comparatively smoother predictions with less oscillatory behaviour. This difference is likely attributable to variations in grid resolution (i.e., finer grids in Star-CCM+ using AMR) and the associated accuracy in capturing complex free-surface dynamics, particularly in the wave-breaking region.

Table 7 Hydrodynamic coefficients: comparison between experimental fluid dynamics (EFD) and CFD results.

| **Parameters** | **EFD** | **Star-CCM+** | **Fluent** |
|---|---|---|---|
| $1000C_T$ | 5.7160 | 5.7370 | 5.7633 |
| $1000C_L$ | 346.7730 | 353.0400 | 352.2221 |
| $1000C_{MY}$ | 1.1540 | 0.9239 | 0.9358 |

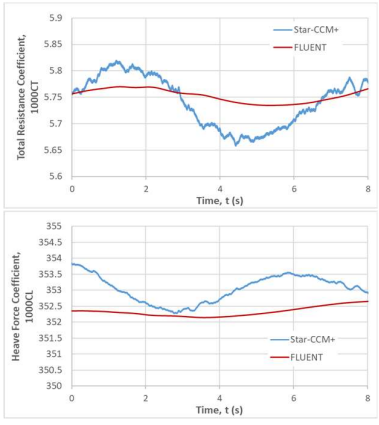


Figure 7 Total resistance coefficient (top), Lift force coefficient (Bottom): comparison between Star-CCM+ and FLUENT.

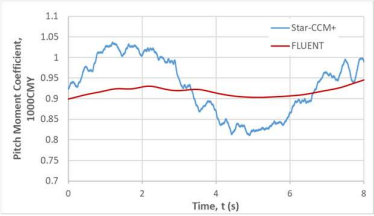


Figure 8 Pitch moment coefficient: comparison between Star-CCM+ and FLUENT.

## 4.2 Mean and RMS Values of Wave Elevation

The mean and root-mean-square (RMS) values of wave elevation were computed to evaluate the statistical characteristics of the free-surface motion around the bow area. This can provide insight into both the average water level and the relative intensities/fluctuations in the unsteady wave breaking. From the CFD codes, the top and bottom wave profiles [1] were extracted separately by following the case description as illustrated in Figure 9. This approach enabled the visualization of complex flow patterns in the wave-breaking region, including plunging waves and air-pocket formation.

Considering that the experimental results are averaged without distinction between top and bottom elevation, the simulated wave elevation from both Star-CCM+ and FLUENT are generally well aligned, particularly the mean values. However, Star-CCM+ predicted higher RMS values over a broader area compared to FLUENT in both the top and bottom elevation. In contrast, FLUENT exhibited notably smaller RMS values, particularly showing much smaller areas of high RMS values around 0.0008.

The numerical analysis predicted the presence of air tubes or cavities, wave crests, jets, and plunging events, which are illustrated using 3D surfaces as shown in Figure 10. In this figure, the four transverse wave slices at non-dimensionalized positions of 0.065, 0.084, 0.103, and 0.122 are also included. These numerical predictions were qualitatively compared with photographs obtained from the physical model tests. It was observed that Star-CCM+ captured a broader bow wave breaking region, closely matching the area highlighted by the red box in the model test photograph.

In addition to the mean and RMS wave elevations, specific wave cuts were extracted at four different locations for quantitative comparison. In this paper, results from only two sections (0.103 and 0.302) are presented as shown in Figure 11 and Figure 12. For both locations, the mean wave elevation predictions from Star-CCM+ are closer to the EFD results. However, the RMS values from Star-CCM+ exhibit slightly larger scatter, regardless of whether the top or bottom profile is considered.

By comparing the top and bottom mean wave-elevation profiles, the location of the air pocket can be determined. Elevated RMS values are indicative of stronger unsteadiness or more intense wave-breaking activity over time. As shown in Figure 13, the air pocket is situated between 0.05 and 0.08, where both CFD codes predict high unsteadiness. Star-CCM+ generates a broader spray region characterized by high unsteadiness, while FLUENT predicts a more pronounced plunging wave, exhibiting a steeper yet smoother circular air cavity.

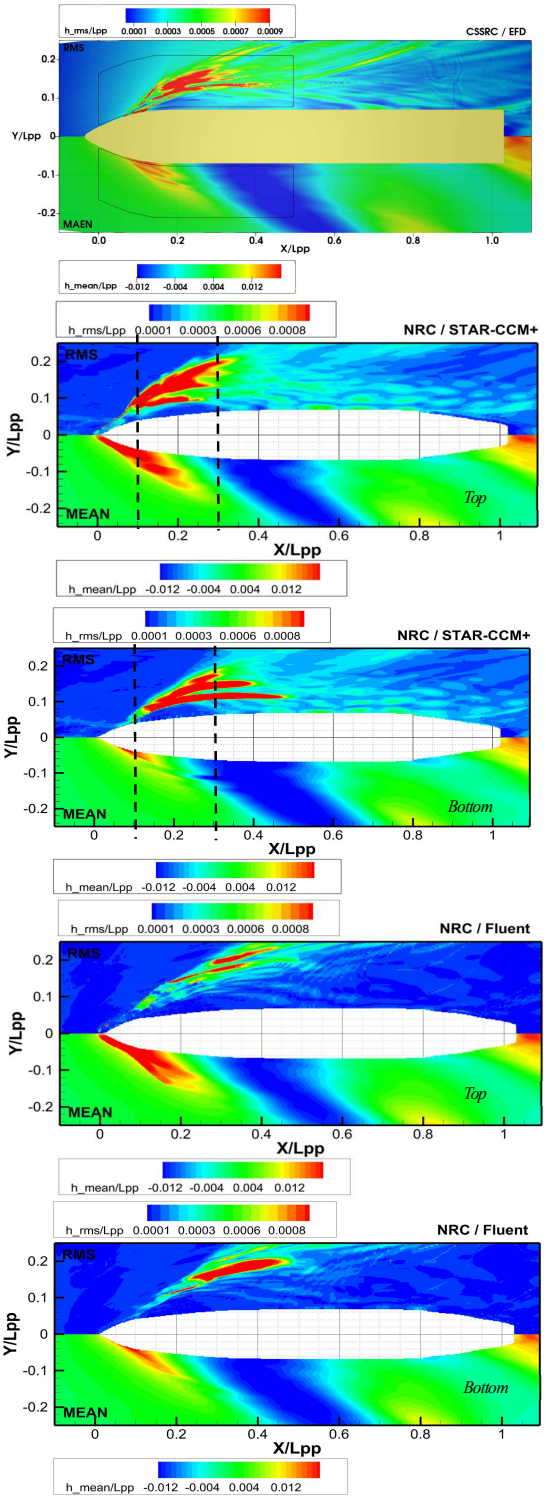


Figure 9 Comparison between EFD and CFD results for top and bottom RMS and mean wave elevation.

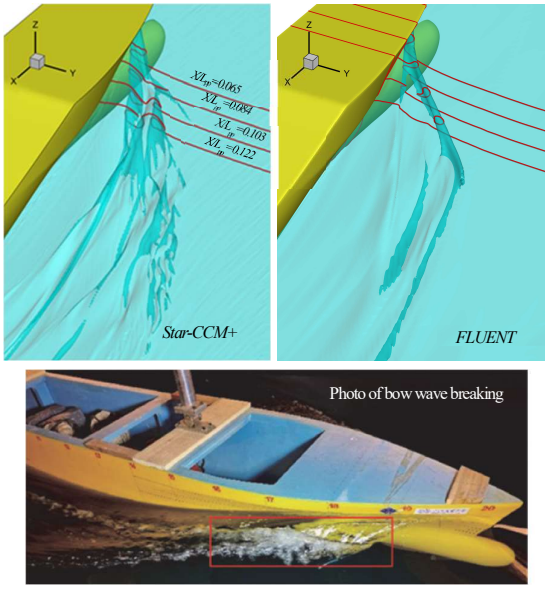


Figure 10 Air tubes at Iso-surface and image of bow wave breaking [12].

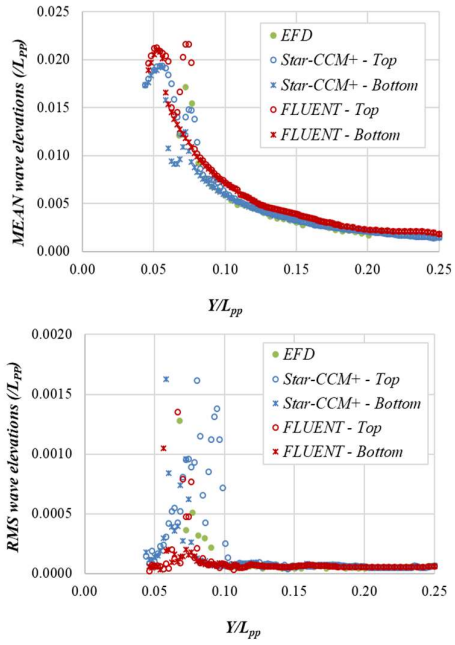


Figure 11 Mean and RMS wave elevation at wave cut $X/L_{PP}=0.103$.

This difference is also observed in the 3D wave contour visualized in the third wave cuts in Figure 10 and the instantaneous wave slice as shown in Figure 13.

When comparing both locations in Figure 11 and Figure 12, the propagation of wave breaking and movement of the air tube can be observed. At the section of 0.103 in Figure 11, both CFD codes indicate that the RMS peaks are concentrated close to the hull, at approximately 0.06, accompanied by larger fluctuations in RMS values. However, at the section of 0.302, located closer to midship, the air tubes and jets appear to shift away from the hull, reaching around 0.17.

Overall, Star-CCM+ captured the air-tube structures and wave-breaking patterns more accurately than FLUENT. It should be noted, however, that the developed CFD models differed, particularly in terms of grid resolution, which may have influenced the results.

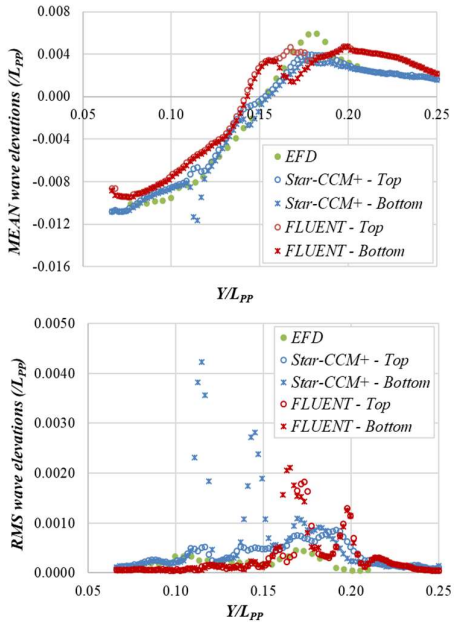


Figure 12 Mean and RMS wave elevation at wave cut $X/L_{PP}=0.302$.

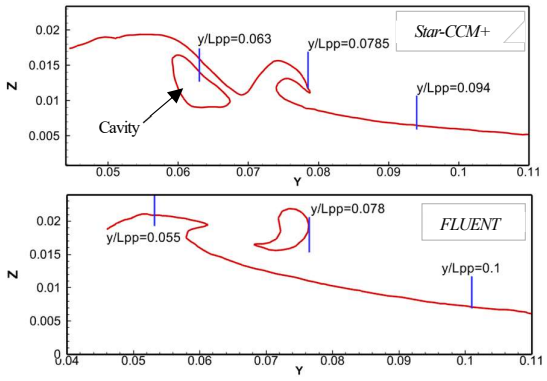


Figure 13 Instantaneous wave profile at $X/L_{PP}=0.103$.

## 4.3 Velocity and Axial Vorticity Distribution

Previous researches have reported violent wave breaking near the bow of the KCS hull, leading to the formation of localized vortex structures. Figure 14 and Figure 15 present the simulated 3D vortex structures near the bow. Two vortex identification methods, the $Q$ and OmegaR ($\Omega_R$) criterion, were applied. In this study, the $\Omega_R$ criterion states the $X$-direction vorticity by following the provided case description. The present study successfully captured localized vortex structures in the bow-wave-breaking region. It was observed that small positive vortex structures were initially generated

by the overturning waves, followed by subsequent negative vortex structures extending over a larger area. As shown in both figures, Star-CCM+ predicted a larger vortex structure propagating toward the midship region, whereas FLUENT produced simpler/smaller vortex structures. This difference is primarily related to the different grid resolutions rather than differences in the applied numerical schemes, as briefly noted in the previous section. However, a more systematic comparison will be required to confirm this.

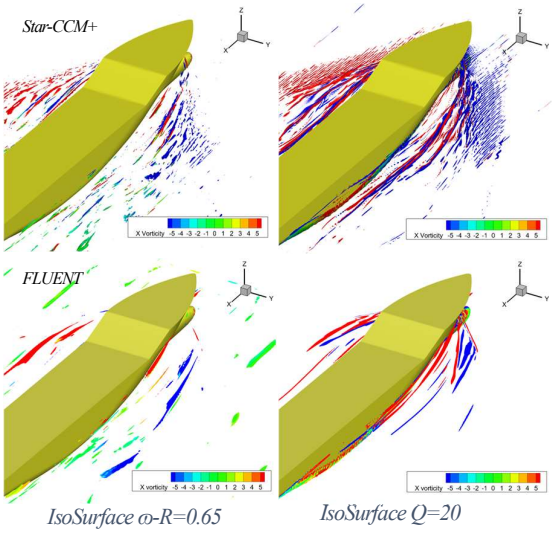


Figure 14 Perspective view of simulated vortex structures near bow (Top: Star-CCM+, Bottom: Fluent).

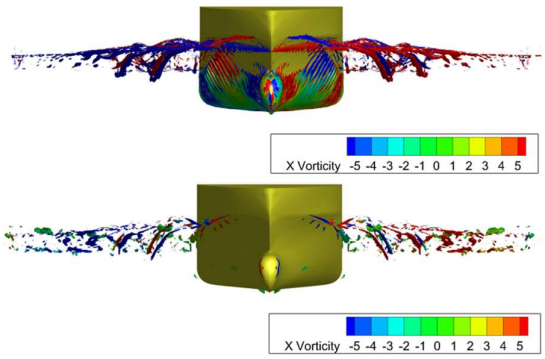


Figure 15 Front view of vortex structure (Star-CCM+).

The longitudinal, lateral, and vertical velocity components (i.e., u, v and w velocity) and the longitudinal vorticity (X-Vorticity) distributions and at three transverse sections *X/L*$_{PP}$*=0.151, 0.199 and 0.302* were estimated through CFD analysis and compared with the physical model test data. It should be noted that all velocities and vorticities were extracted as instantaneous values instead of taking time averaged quantities. All velocity components were normalized by the tested ship speed. The results from two transverse sections are presented from Figure 16 to Figure 18. Overall, good agreement is observed between the CSSRC measurements and the CFD predictions, with Star-CCM+ showing closer alignment to the experimental data.

From Figure 16 and Figure 17, along the transverse wave slice at *X/L*$_{pp}$ *= 0.151*, the Star-CCM+ prediction indicates the presence of an air tube around *Y/L*$_{pp}$ *= 0.082*, the formation of a jet from the first overturning wave at *Y/L*$_{pp}$ *= 0.098*, and the crest and jet associated with the second overturning wave at *Y/L*$_{pp}$ *= 0.15*. The figure also shows that the longitudinal and vertical velocity components have a direct correlation with the longitudinal vorticity distribution.

Figure 18 shows the presence of smaller air tubes and overturning waves located away from the hull, accompanied by a lower amplitude of negative longitudinal vorticity. No significant wave breaking events were observed along this section, and no pronounced longitudinal vorticity was identified. Overall, a reasonable level of agreement was achieved between the experimental measurements and the CFD predictions.

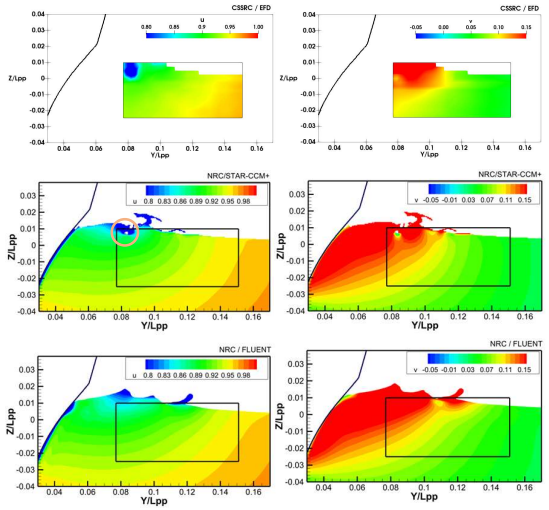


Figure 16 EFD and CFD results for longitudinal (left) and lateral (right) velocities at *X/L*$_{PP}$*=0.151*.

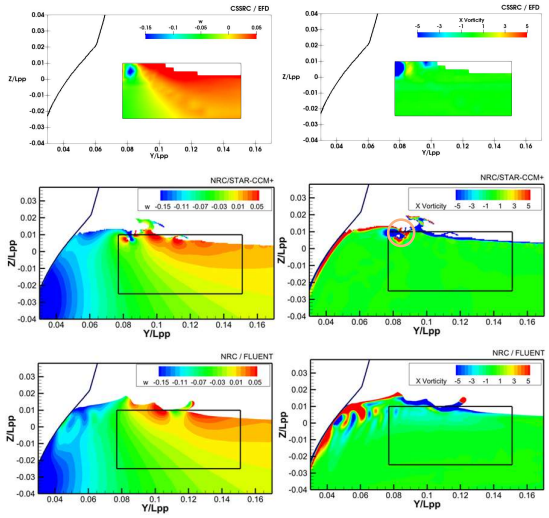


Figure 17 EFD and CFD results for vertical velocity (left) and longitudinal vorticity (right) at *X/L*$_{PP}$*=0.151*.

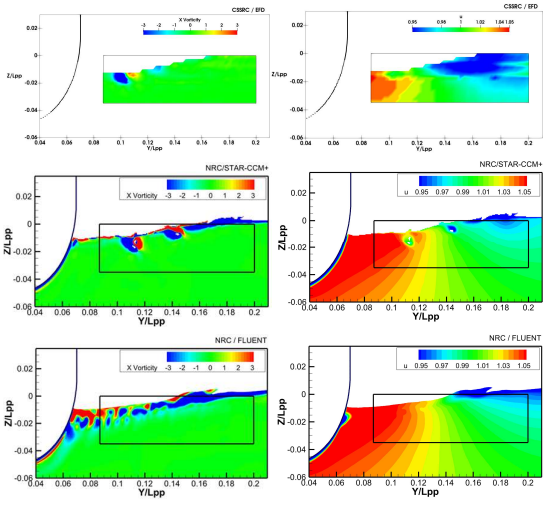


Figure 18 Comparison of EFD and CFD results for longitudinal vorticity (left) and longitudinal velocity (right) at $X/L_{PP}=0.302$.

## 5. CONCLUSION

The present study investigated the bow wave breaking characteristics of the KCS hull at $Fr=0.35$ through numerical analysis, with the aim of producing a dataset for the W2025 CFD workshop. CFD simulations were carried out using two commercial solvers, Star-CCM+ and FLUENT. URANS simulation was conducted with the SST $k$-$\omega$ turbulence model. In addition to validating the numerical results against the measurement data provided by CSSRC, a comparative evaluation of the predictions from both CFD packages was performed. The key findings from this study are summarized below:

- CFD predictions demonstrated reasonable agreement with the experimental measurements. However, both CFD solvers significantly underpredicted the pitch moment compared with the resistance and heave force.
- The Star-CCM+ model with Adaptive Mesh Refinement captured wave-breaking phenomena more accurately than the FLUENT model with coarse meshes, showing closer resemblance to the experimental results. However, further systematic analysis is required, as the FLUENT simulations were conducted without dynamic grid refinement capabilities due to limited computing resources.
- Both CFD analyses indicated that differences between the top and bottom RMS and mean wave elevations near the bow reflect the degree of unsteadiness and fluctuations associated with wave breaking.
- From the transverse wave cuts near the bow, the presence of air tubes, crest, jet and plunging caused by overturning waves were successfully captured.
- The velocity components and the axial vorticity along the transverse wave slice sections shows the violent wave breaking and the longitudinal and vertical velocity components have direct impact on $X$-vorticity generations.

## REFERENCES


[1] "KCS Wave Breaking", Workshop on CFD in Ship Hydrodynamics

[2] Baba, E., "A New Component of Viscous Resistance of Ships," Journal of the Society Naval Architects of Japan, volume 125, pp. 9–34, 1969.

[3] Hengelmolen, V. and Wellens, P. R., "An experimental study on added resistance focused on the effects of bow wave breaking and relative wave Measurements", International Shipbuilding Progress, volume 69, pp. 61-89, 2022, DOI 10.3233/ISP-210018.

[4] Choi, B., Wellens, P. R. and Huijsmans, R. H. M., "Experimental assessment of effects of bow-wave breaking on added resistance for the fast ship", International Shipbuilding Progress, volume 66, pp. 111-143, 2019, DOI.org/10.3233/ISP-180242.

[5] Mascio A. D., Muscari R, Broglia R., "Computation of free surface flows around ship hulls by a level set approach", Proceedings of the 8th International Conference on Numerical Ship Hydrodynamics, Busan, South Korea, 2003.

[6] Olinieri. A., Pistani, F., Wilson, R., Campana, E. F. and Stern, F., "Scars and Vortices Induced by Ship Bow and Shoulder Wave Breaking", Journal of Fluid Engineering, Volume 129, November, 2007.

[7] Wilson, R. V., Carrica, P. M. and Stern, F., "URANS Simulations for a High-speed Transom Stern Ship with Breaking Waves", International Journal of Computational Fluid Dynamics, volume 20 (2), pp. 105-125, February, 2006.

[8] Lin, C. and Percival, S., "Free surface viscous flow computation around a transom stern ship by chimera overlapping scheme", Proceedings of the 23rd ONR Symposium on Naval Hydrodynamics, September 2000.

[9] Wang, W., Qiu G., Wang J., and Wan D., "Experimental and Computational Investigations on KCS Wave Breaking with Trim and Sinkage Variation", 14th ISOPE Pacific-Asia Offshore Mechanics Symposium, pp. 434–440, Nov. 2020.

[10] Xu, Y., Sun, P., Guan, X. Peng, Y, Liu, N. and Zang, X., "Numerical Study on the Breaking Bow Wave of High-speed KCS Model based on Smoothed Particle Hydrodynamics Methods, Journal of Marine Science and Application, volume 23, pp. 723-733, 2024.

[11] Simonsen, C. D., Otzen, J. F., Joncquez, S. and Stern, F., "EFD and CFD for KCS Heaving and Pitching in Regular Head Wave", Journal of Marine Science and Technology, volume 18, 2013.

[12] Li, X., Bao, F., Wang, J., Wan, D. and Xu, J., "Spectral and Statistical Analysis of Bow Wave Breaking Characteristics of KCS Ship", Journal of Hydrodynamics, volume 36 (4), 2024.